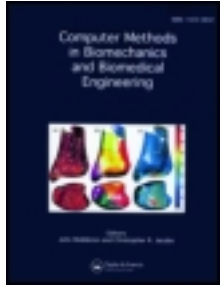


This article was downloaded by: [171.65.102.222]

On: 28 November 2012, At: 14:50

Publisher: Taylor & Francis

Informa Ltd Registered in England and Wales Registered Number: 1072954 Registered office: Mortimer House, 37-41 Mortimer Street, London W1T 3JH, UK



Computer Methods in Biomechanics and Biomedical Engineering

Publication details, including instructions for authors and subscription information:

<http://www.tandfonline.com/loi/gcmb20>

3D finite element models of shoulder muscles for computing lines of actions and moment arms

Joshua D. Webb^a, Silvia S. Blemker^{b c d} & Scott L. Delp^{a e}

^a Department of Mechanical Engineering, Stanford University, Stanford, CA, 94305, USA

^b Department of Mechanical and Aerospace Engineering, University of Virginia, Charlottesville, VA, 22904, USA

^c Department of Biomedical Engineering, University of Virginia, Charlottesville, VA, 22904, USA

^d Department of Orthopaedic Surgery, University of Virginia, Charlottesville, VA, 22904, USA

^e Department of Bioengineering, Stanford University, Stanford, CA, 94305, USA

Version of record first published: 20 Sep 2012.

To cite this article: Joshua D. Webb, Silvia S. Blemker & Scott L. Delp (2012): 3D finite element models of shoulder muscles for computing lines of actions and moment arms, *Computer Methods in Biomechanics and Biomedical Engineering*, DOI:10.1080/10255842.2012.719605

To link to this article: <http://dx.doi.org/10.1080/10255842.2012.719605>



PLEASE SCROLL DOWN FOR ARTICLE

Full terms and conditions of use: <http://www.tandfonline.com/page/terms-and-conditions>

This article may be used for research, teaching, and private study purposes. Any substantial or systematic reproduction, redistribution, reselling, loan, sub-licensing, systematic supply, or distribution in any form to anyone is expressly forbidden.

The publisher does not give any warranty express or implied or make any representation that the contents will be complete or accurate or up to date. The accuracy of any instructions, formulae, and drug doses should be independently verified with primary sources. The publisher shall not be liable for any loss, actions, claims, proceedings, demand, or costs or damages whatsoever or howsoever caused arising directly or indirectly in connection with or arising out of the use of this material.

3D finite element models of shoulder muscles for computing lines of actions and moment arms

Joshua D. Webb^a, Silvia S. Blemker^{b,c,d} and Scott L. Delp^{a,e,*}

^aDepartment of Mechanical Engineering, Stanford University, Stanford, CA 94305, USA; ^bDepartment of Mechanical and Aerospace Engineering, University of Virginia, Charlottesville, VA 22904, USA; ^cDepartment of Biomedical Engineering, University of Virginia, Charlottesville, VA 22904, USA; ^dDepartment of Orthopaedic Surgery, University of Virginia, Charlottesville, VA 22904, USA; ^eDepartment of Bioengineering, Stanford University, Stanford, CA 94305, USA

(Received 17 December 2011; final version received 6 August 2012)

Accurate representation of musculoskeletal geometry is needed to characterise the function of shoulder muscles. Previous models of shoulder muscles have represented muscle geometry as a collection of line segments, making it difficult to account for the large attachment areas, muscle–muscle interactions and complex muscle fibre trajectories typical of shoulder muscles. To better represent shoulder muscle geometry, we developed 3D finite element models of the deltoid and rotator cuff muscles and used the models to examine muscle function. Muscle fibre paths within the muscles were approximated, and moment arms were calculated for two motions: thoracohumeral abduction and internal/external rotation. We found that muscle fibre moment arms varied substantially across each muscle. For example, supraspinatus is considered a weak external rotator, but the 3D model of supraspinatus showed that the anterior fibres provide substantial internal rotation while the posterior fibres act as external rotators. Including the effects of large attachment regions and 3D mechanical interactions of muscle fibres constrains muscle motion, generates more realistic muscle paths and allows deeper analysis of shoulder muscle function.

Keywords: rotator cuff; deltoid; 3D finite element muscle model; musculoskeletal model, shoulder biomechanics

Introduction

Musculoskeletal models of the shoulder typically represent muscle lines of action as a collection of line segments (van der Helm 1994; Garner and Pandy 2001; Holzbaur et al. 2005). These models have been useful for a wide variety of applications including simulating surgical procedures (Holzbaur et al. 2005), investigating wheelchair mechanics (van der Helm and Veeger 1996; van der Woude et al. 2001) and controlling neuroprostheses (Hincapie et al. 2008; Blana et al. 2009). However, shoulder muscles have characteristics that make them challenging to represent using line-segment representations. Shoulder muscles have broad attachment areas, complex fibre arrangements and paths that wrap over other muscles and bones. These anatomical features affect muscle actions and may not be accurately represented with line-segment approximations.

For muscles with broad attachments, a single line of action is generally insufficient to represent the geometry, so multiple lines of action must be defined (Van der Helm and Veenbaas 1991). This approximation makes model creation difficult because one must decide how many lines of action (compartments) to use, where to place the origin, insertion and path of each compartment and how to estimate the muscle and tendon parameters (e.g. optimal

fibre length, maximum isometric force and so on) for each compartment.

The deltoid and rotator cuff muscles have complex arrangements of fibres and multiple functional compartments (Ward et al. 2006). It is possible to represent multiple compartments of a muscle with separate lines of action, but line-segment models assume that all fibres within a compartment deform uniformly and independently of neighbouring compartments. Imaging (Pappas et al. 2002; Blemker et al. 2007; Zhou and Novotny 2007) and computational studies (Yucesoy et al. 2003; Blemker et al. 2005; Blemker and Delp 2006; Epstein et al. 2006) have demonstrated that deformations can be non-uniform within muscles, and biomechanical experiments have demonstrated that adjacent muscle compartments are not mechanically independent (Huijing 1999; Huijing and Baan 2001; Maas et al. 2001).

Shoulder muscles wrap over each other and other surrounding tissues; therefore, to accurately represent shoulder muscle geometry, it is important to represent muscle–muscle and muscle–bone interactions. Line-segment models use geometrical constraints, such as ‘via points’ or wrapping surfaces (Blemker and Delp 2005), to represent contact with surrounding tissues. Prescribing these geometrical constraints is challenging because it requires knowledge of how muscles deform in three dimensions.

*Corresponding author. Email: delp@stanford.edu

Three-dimensional (3D) finite element modelling allows representation of muscles with broad attachment regions, incorporation of complex fibre trajectories and modelling of contact between muscles and surrounding structures based on their physical interactions (Fernandez et al. 2004; Blemker and Delp 2005; Lemos et al. 2008; Oberhofer et al. 2009; Lu et al. 2011). The goals of this study were to (i) develop and test 3D finite element models of the deltoid and rotator cuff muscles and tendons to investigate how moment arms vary across the fibres within each muscle and (ii) compare the 3D models with line-segment representations to study how predictions of shoulder muscle moment arms differ between the two types of models.

Methods

The 3D models of the shoulder muscles were constructed from magnetic resonance images (MRIs) of a single healthy subject. The MRIs were segmented to define the anatomical structures, and a finite element mesh was fit to each structure. Bones were represented as rigid bodies. Muscles and tendons were represented using a nearly incompressible, hyperelastic, transversely isotropic constitutive model (Blemker and Delp 2005). Fibre maps that represent the 3D trajectories of the fibres were constructed for each muscle (Blemker and Delp 2005). The kinematics for shoulder abduction and shoulder rotation were prescribed as input to the finite element simulations, and the resulting muscle deformations were predicted. The fibre deformations were tracked through the finite element solutions, and a moment arm was calculated for each fibre at each joint angle. Analysis of the fibre moment arms provided insights into the function of the muscles.

Imaging and geometry

A 26-year-old subject with no history of shoulder pathologies or injuries (height: 1.75 m, weight: 80 kg) provided informed consent in accordance with the Institutional Review Board at Stanford University, and was imaged in a supine position with arms at his sides in a 1.5 T MRI scanner (GE Healthcare, Milwaukee, WI, USA) using a body coil. Image parameters were chosen to maximise the contrast at muscle boundaries. We used two imaging protocols: one for the rotator cuff and another for the deltoid and bones. The rotator cuff was imaged using an oblique sagittal imaging plane and a 2D fast spin echo sequence (20 cm \times 20 cm field of view, 2.5 mm slice thickness, 1 mm space between slices, repetition time (TR) 4200 ms, echo time (TE) 13.4 ms, in plane resolution 0.78 mm, flip angle 90°). Images were acquired from the lateral edge of the shoulder to the medial border of the scapula. The deltoid and bones were imaged using an axial

image plane. A 3D spoiled gradient sequence was used for this series (40 cm \times 40 cm field of view, 3 mm slice thickness, TR 11.64 ms, TE 5.3 ms, in plane resolution 0.78 mm, flip angle 30°). Images were acquired from approximately the fourth cervical vertebra to the distal end of the humerus. Surfaces of the muscles, tendons and bones were defined by manually outlining the boundaries of each tissue on each image (3D Doctor, Able Software, Lexington, MA, USA). These outlines were used to create 3D surfaces representing the anatomical structures. The surfaces were imported into Truegrid (XYZ Scientific, Livermore, CA, USA), a finite element mesh generator. A finite element mesh was constructed for each muscle–tendon unit (Figure 1). Muscle geometry and tendon geometry were represented with eight-node, linear hexahedral elements, and bone surfaces were represented as rigid linear triangular surface elements (Table 1).

To define the 3D trajectories of fibres within each 3D muscle model, we used a mapping technique that applies a muscle fibre template to the finite element mesh (Blemker and Delp 2005). This process involves creating a fibre template (in which the fibres describe Bezier splines contained within a unit cube), and then mapping the fibre template to fit the volume of the MRI-based muscle mesh. The fibre template is embedded within a finite element mesh that has the same number of elements and nodes as the MRI-based muscle mesh. Because of this one-to-one correspondence of the two meshes, it is possible to map the points in the fibre map from the template mesh to the geometry of the muscle. Each muscle was divided into three regions (anterior to internal tendon, middle and posterior to internal tendon), where the fibre map was defined such that the fibres originated along the proximal tendons and inserted along the distal tendons (Figure 2). Each region was represented with a ‘fanned’ fibre map (Blemker and Delp 2005) with control points chosen to replicate the fibre directions observed in photographs taken from dissected shoulder muscles. The trajectories and regions of fibres in the model agreed with those described by Ward et al. (2006) and Kim et al. (2007). Based on the fibre trajectories, a fibre direction vector was determined for each element in the mesh to serve as an input to the constitutive model.

Tissue interactions

The muscle and tendon meshes were connected using a continuous mesh with shared nodes between them. The tendon–bone interface was represented by rigidly attaching the element faces of the tendon to the bone surface. For all contact interfaces, we used a penalty-based method (Hallquist et al. 1985) with a penalty scale factor of 0.1. We then used an augmented Lagrangian algorithm (Laursen and Maker 1995) to reduce the penetration of the surfaces. Bones were defined as rigid, and a single pass

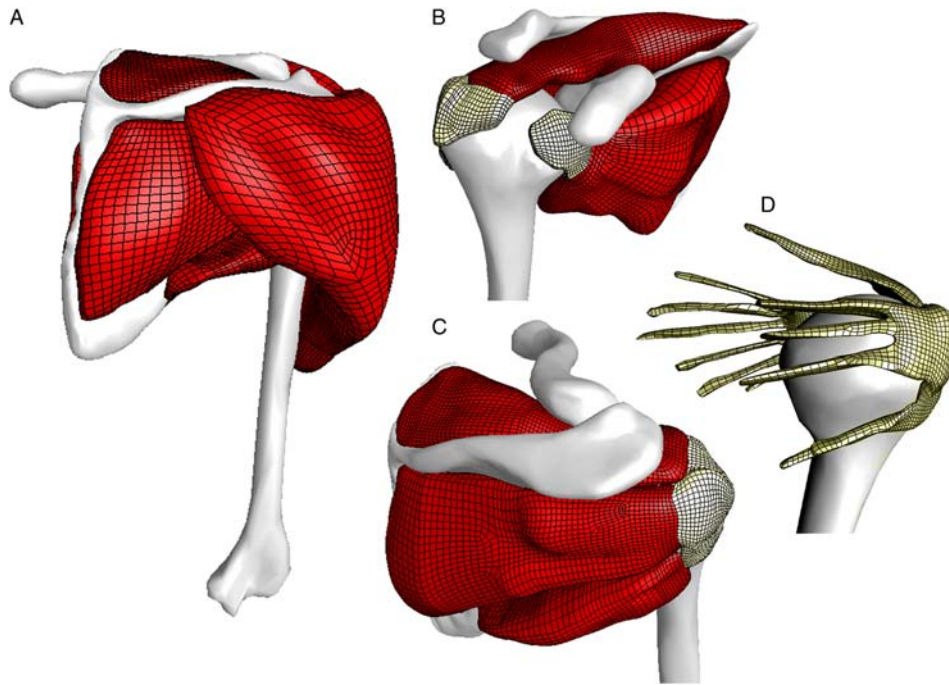


Figure 1. Finite element model of the shoulder musculoskeletal system. (A) Posterior view illustrating the models of the deltoid and rotator cuff muscles. (B) Anterior view of the rotator cuff with the deltoid and clavicle removed illustrating subscapularis and supraspinatus. (C) Posterior view of the rotator cuff with the deltoid removed illustrating infraspinatus and teres minor. (D) Posterior view of rotator cuff tendons attached to the humeral head.

algorithm was used between the bones and muscles, with the bone defined as the master contact surface. For muscle–muscle and muscle–tendon contact, a two-pass algorithm was used with the deeper muscle considered to be the master surface, and the superficial muscle was chosen as the slave surface.

Constitutive model

We used a nearly incompressible, hyperelastic, transversely isotropic constitutive model (Weiss et al. 1996; Criscione et al. 2001; Blemker and Delp 2005) to characterise the nonlinear stress–strain relationship of muscle and tendon (Table 2). This constitutive model characterises the active and passive behaviour of the muscle along the direction of muscle fibres based on the

force–length relationship of a sarcomere (Zajac 1989), with a specified activation level between 0 and 1. The model also includes the contributions of strain energy for shear deformations in the plane transverse to fibres and between adjacent fibres. Tendons were modelled with the same material model, but with different parameters that describe their along-fibre and cross-fibre properties

Table 1. Summary of the nodes and elements in the finite element model.

Muscle	Nodes	Elements	# Tendon branches
Supraspinatus	26,138	23,610	1
Infraspinatus	21,320	19,119	3
Teres minor	14,358	12,848	2
Subscapularis	20,091	17,899	6
Deltoid	15,972	14,088	0
Bones	7436	14,860	NA
Total	105,315	87,564	NA

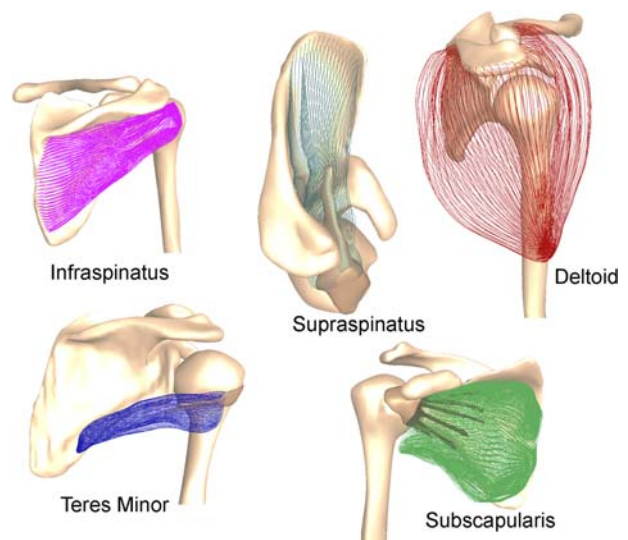


Figure 2. 3D fibre trajectories for each of the shoulder muscles.

Table 2. Input parameters for the transversely isotropic material model used to represent muscle and tendon.

Material parameter	Muscle (Pa)	Tendon (Pa)	Form
Along fibre stretch, λ	Piecewise-quadratic	Exponential	$W_1 = f(\text{activation}, \lambda)$
Along fibre shear modulus, G_1	500	50,000	$W_2 = G_1 \phi^2$
Cross-fibre shear modulus, G_2	500	50,000	$W_3 = G_2 \phi^2$
Bulk modulus, K	10E7	10E9	$W_4 = K [\ln(J)]^2$
Strain energy density = $\Phi = W_1 + W_2 + W_3 + W_4$			

(Table 2). A complete description can be found in Blemker et al. (2005).

Finite element simulations and computation of fibre moment arms

The three rotations of the humerus were prescribed, and the motions of the scapula and clavicle were determined based on regression Equations (de Groot and Brand 2001). The glenohumeral joint was represented as a ball-and-socket joint, and the rotation centre was determined by fitting a sphere to the articulating surface of the humeral head (Van der Helm et al. 1992; Meskers et al. 1998). Bony landmarks were digitised, and bone axes were defined in accordance with the recommendations of the International Society of Biomechanics (de Groot and Brand 2001; Wu et al. 2005).

We simulated two motions of the shoulder. The first motion ranged from 0° to 90° of thoracohumeral abduction. The second motion ranged from 45° of internal rotation to 45° of external rotation with the abduction angle fixed at 0°. To analyse each muscle's action for each of these motions, we prescribed each of the two motions (in 1° increments) while applying a moderate level of activation for each muscle (10–30% of maximum for abduction and 5–10% of maximum for rotation). Simulations were run quasi-statically using Nike3D (version 3.4.1), an implicit finite element solver (Puso et al. 2006), on a Workstation (Dell, dual quad-core Xeon processor, 20 Gb RAM) and took 12–20 h.

We sampled the fibre maps for each muscle to obtain evenly distributed fibres that we could track throughout a simulation, and computed the fibre's length as a function of thoracohumeral angle. The moment arm for each muscle fibre was determined using the principle of virtual work (An et al. 1984; Hughes et al. 1998): $ma_f = (dl_f)/(d\theta)$, where dl_f is the change in length of the muscle fibre and $d\theta$ is the change in thoracohumeral angle. Differentiation was made using a second-order central difference algorithm, and the moment arms were then smoothed using a second-order, low-pass Butterworth filter with a cut-off frequency of 1 rad^{-1} . We compared the fibre moment arms predicted by the 3D models with moment arms determined experimentally (An et al. 1984; Otis et al. 1994; Liu et al. 1997; Gatti et al. 2007; Lu et al. 2011) and from a model of the upper

extremity with line-segment representations of the muscle (Holzbaur et al. 2005).

Results

Abduction moment arms

The abduction moment arms of the muscle fibres within each muscle vary substantially (Figure 3). Supraspinatus fibre moment arms range from 1.0 to 2.0 cm at neutral position (0° abduction) and from 0.3 to 1.0 cm at 90° of abduction (Figure 3(A)). The model of the upper extremity that uses line segments (Holzbaur et al. 2005) for this muscle has a moment arm similar in magnitude to the 3D model, but that changes more with shoulder abduction angle. The abduction moment arm is nearly zero in the line-segment model when the shoulder is abducted, but the finite element model reveals that the moment arm is maintained with abduction.

Infraspinatus moment arms vary from 1.2 cm adduction to 1.3 cm abduction at 0° of abduction (Figure 3(B)). The fibres with adduction moment arms are located on the inferior portion of the muscle. The line-segment-based model (Holzbaur et al. 2005) predicts that infraspinatus is a weak abductor, while the 3D model predicts that the superior fibres of the muscle are strong abductors, and the inferior fibres are adductors.

Teres minor moment arms vary from 0.0 to 1.4 cm of adduction (Figure 3(C)). Teres minor fibres have a nearly constant adduction moment arm throughout the range of motion, consistent with its insertion on the inferior part of the greater tubercle, below the rotation centre of the humeral head. Teres minor has the smallest cross section and the most parallel fibres of cuff muscles, and it agrees with line-segment representations (Otis et al. 1994; Holzbaur et al. 2005).

Subscapularis moment arms vary from 1.7 cm adduction to 1.0 cm abduction at the neutral position (Figure 3(D)). Abduction moment arms for the subscapularis decrease with abduction angle. The superior fibres of subscapularis are abductors, but the middle and inferior fibres are adductors. The line-segment model (Holzbaur et al. 2005) and experimental data (Liu et al. 1997) predict that the muscle is a weak abductor, whereas the 3D model suggests that a large portion of the muscle contributes to adduction.

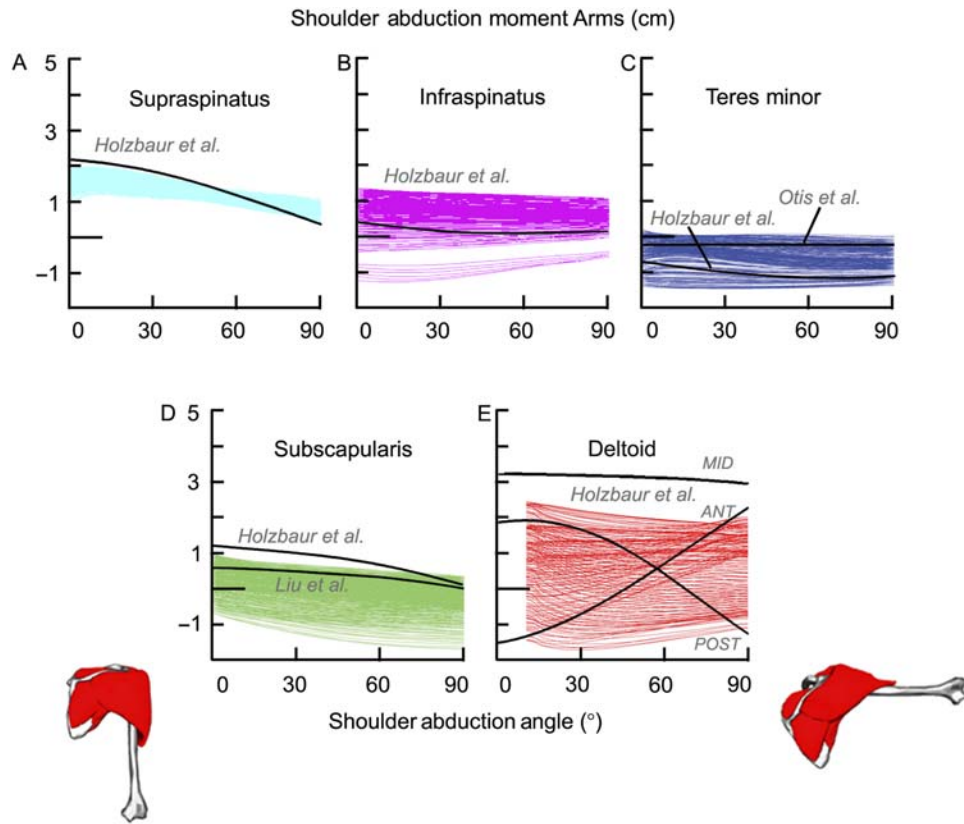


Figure 3. Shoulder abduction moment arms for each fibre in the finite element model of the supraspinatus (A), infraspinatus (B), teres minor (C), subscapularis (D) and deltoid (E) over a range of shoulder abduction angles. Abduction moment arms are positive. Moment arms computed with the model of Holzbaaur et al. (2005), and experimental measurements by Liu et al. (1997) and Otis et al. (1994) are shown for comparison. The moment arms from Liu et al. (1997) are scaled by two-thirds to transform from glenohumeral angle to thoracohumeral angle based on the ratio reported by Inman et al. (1944). ANT, MID and POST in E designate the anterior, middle and posterior lines of action from Holzbaaur et al. (2005).

Deltoid abduction moment arms range from 2.5 cm abduction to 1.2 cm adduction (Figure 3(E)). The fibres in the middle compartment have the largest abduction moment arms, whereas the fibres at the anterior and posterior borders have adduction moment arms. The 3D model agrees with the experimental findings of Liu et al. (1997). The abduction fibre moment arms in the 3D model remain relatively constant with abduction angle, but the line-segment approximation of deltoid (Holzbaaur et al. 2005) predicts that the anterior and posterior deltoid have moment arms that vary greatly with abduction angle (Figure 3(E), grey lines).

Rotation moment arms

Supraspinatus rotation moment arms range from 1.5 cm internal to 0.5 cm external rotation at 45° of internal rotation and from 1.2 cm internal to 1.8 cm external rotation at 45° of external rotation (Figure 4(A)). Anterior fibres remain internal rotators, and posterior fibres remain external rotators throughout the range of motion. The

fibres increase their external rotation potential as the 3D model moves into externally rotated positions.

Infraspinatus moment arms range from 0.2 cm internal to 1.7 cm external rotation at 45° of internal rotation and from 0.2 to 2.5 cm external rotation at 45° of external rotation (Figure 4(B)). External rotation moment arms increase with external rotation angle, giving infraspinatus better leverage in externally rotated positions. The line-segment model (Holzbaaur et al. 2005) predicts an external rotation moment arm as large as the largest moment arm in the 3D model.

Teres minor moment arms vary from 0.5 to 2.2 cm external rotation (Figure 4(C)). The fibres of teres minor function as external rotators throughout the range of motion and slightly increase their external rotation moment arms as the shoulder externally rotates. The rotational action of teres minor is represented well by a line-segment approximation (Holzbaaur et al. 2005).

Subscapularis moment arms vary from 1.0 cm internal to 0.8 cm external rotation at 45° of internal rotation and from 0.3 to 2.5 cm internal rotation at 45° of external

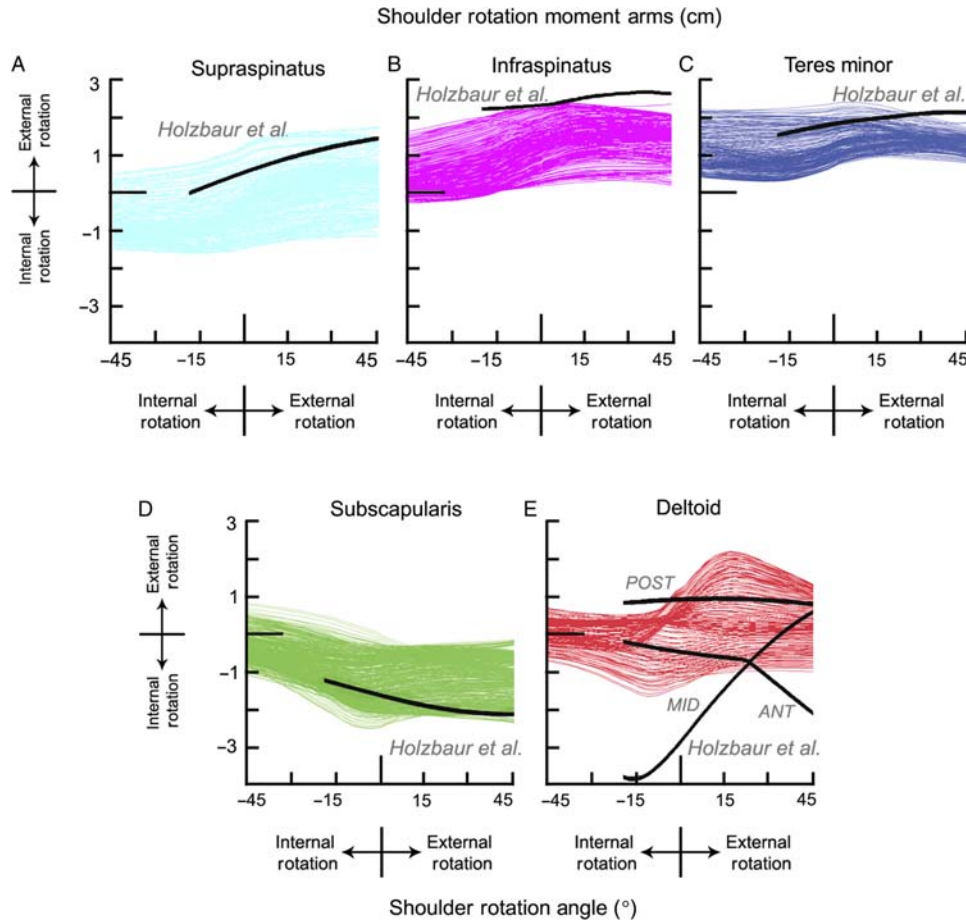


Figure 4. Rotation moment arms for muscle fibres in the finite element model. Rotation occurs at 0° of abduction. Black lines are moment arms calculated by the Holzbaaur et al. (2005) line-segment model.

rotation (Figure 4(D)). The subscapularis moment arms become more internal with increasing external rotation. Although most of the subscapularis fibres act as internal rotators, a few fibres act as external rotators at internally rotated positions. The moment arms calculated by the line-segment model are close to the fibres with the greatest internal rotation fibre moment arm from the 3D model.

At internally rotated positions, the rotation moment arms of the deltoid range from 0.75 cm internal to 0.75 cm external rotation (Figure 4(E)). As the arm externally rotates, the external rotation moment arms of the posterior deltoid fibres increase while the internal rotation moment arms of the anterior fibres remain nearly constant. The posterior deltoid line of action of the line-segment model agrees well with the posterior fibres of the 3D model. However, the moment arms of the middle and anterior lines in the line-segment model vary more with shoulder rotation angle than those predicted by the 3D model.

Discussion

Our comparisons of 3D finite element models to line-segment models of the same muscles revealed two important differences. First, the line-segment models underconstrained the muscle paths in some cases; therefore, the moment arms computed with the line-segment models changed more with joint rotation than moment arms computed with the 3D models. Second, the 3D models predicted substantial variability in moment arms across fibres within each muscle; this feature was not generally represented in line-segment models.

The lack of adequate constraint provided by a line-segment model was prominent in the deltoid, a muscle represented by three compartments. When line-segment models separate muscles into compartments, the compartments are assumed to be mechanically independent, and their paths can move freely with respect to one another. A comparison of the line-segment-based deltoid model and the 3D deltoid model demonstrates how the motions of the middle fibres are constrained by the interactions with

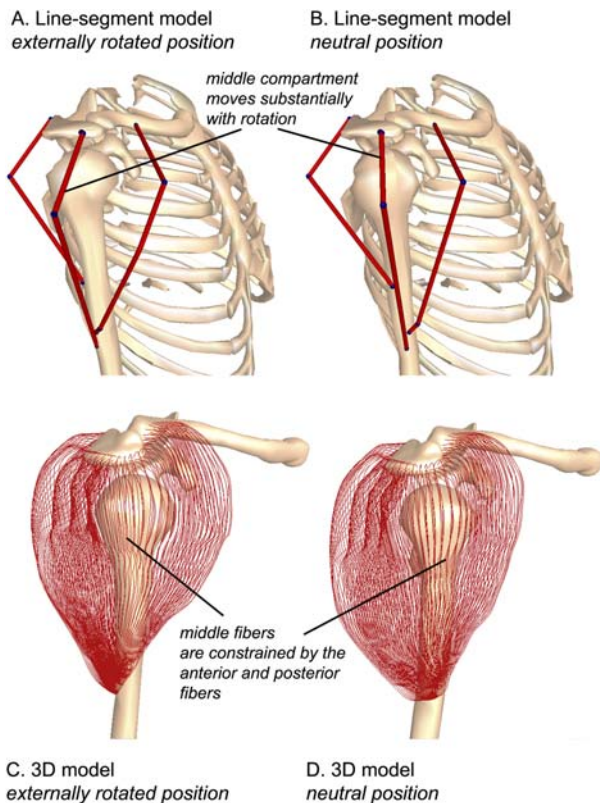


Figure 5. Comparison of muscle paths for a line-segment model of the deltoid (A, B) and the 3D finite element model of the deltoid (C, D) over a range of shoulder rotation (45° external rotation (A, C) to neutral (B, D)). When the humerus is externally rotated, the middle compartment of the line-segment model slides posteriorly. In contrast, the 3D muscle model fibres displace only slightly between the two positions due to the constraints associated with the mechanical interaction between compartments and preservation of muscle volume.

the neighbouring muscle tissue in the 3D model, but the middle compartment path moves freely without constraints in the line-segment model (Figure 5). Although via points of a line-segment model could represent these constraints, it is difficult to define via points to constrain the path for all motions of the shoulder.

Muscle fibre moment arms vary substantially within each of the shoulder muscles studied. For some muscles, the variation was more than the mean moment arm. This variation occurs because the rotator cuff muscles have fibres that span the joint (in contrast to other muscles in which the tendons span the joint). The high degree of variability in moment arms across fibres could affect force-generating capacity of these muscles; variable fibre excursions suggest that the fibres operate on different regions of the force-length curve. Variable fibre moment arms also indicate that strains are non-uniform within these muscles during joint motions, as has been demonstrated in an imaging study of the rotator cuff (Zhou and Novotny 2007).

Contact and wrapping play important roles in shoulder muscle deformations. Line-segment models interact with wrapping surfaces to capture the effects of underlying structures, but discontinuities in moment arms often occur when muscle lines of action intersect a wrapping surface (e.g. see the anterior fibres of the deltoid in external rotation, Figure 4(E)). The 3D models allow smooth representation of contact between muscles, tendons and bones without via points, wrapping surfaces or discontinuities.

The higher fidelity descriptions of muscle paths provided by 3D finite element models of shoulder muscles come at a high computational cost. A finite element model can take up to 20 h to simulate a simple motion. In contrast, line-segment models can be controlled in real time, an important feature for time-sensitive applications such as neuroprosthetic control (Blana et al. 2008). Halloran et al. (2009, 2010) developed a surrogate modelling approach that enables efficient concurrent simulation of finite element models and forward dynamic models. Extension of these techniques to 3D finite element muscle models would expand the applicability of the 3D shoulder muscle models described here. The computational cost and complexity of meshing shoulder muscles and tendons make conduction of a thorough mesh convergence analysis difficult with current meshing tools and computational resources. Mesh refinement would likely affect the localised element-by-element strain and stress predictions of these models. However, we would not expect refinement to affect the overall fibre moment arm predictions that form the basis of our conclusions, since each of the representative fibre moment arm predictions is a result of the integration of behaviour across roughly 500–1000 elements.

3D muscle models require more input data than line-segment models. For example, the 3D models require specification of the spatial arrangement of fibre directions. To provide a detailed description of the fibre directions, we used a mapping method that incorporates knowledge of each muscle's architecture, along with specification of the areas of muscle origin and insertion. Our fibre maps are in agreement with measurements by Ward et al. (2006) and Kim et al. (2007) in cadavers. In the future, refinements of diffusion tensor imaging techniques (Napadow et al. 2001; Galban et al. 2004; Prompers et al. 2006) may provide *in vivo* measurements of fibre trajectories. To provide an initialised state of our models, we assumed that all areas of the muscle tissue were at a zero strain state in the original model configuration. Future experimental measurements of distributions of initial stretches within fibres throughout these muscles [perhaps by measurement of *in vivo* sarcomere length distributions (Llewellyn et al. 2008)] would provide the necessary data to describe the distribution of initial fibre stretches for these models. Although we do not expect this information to influence the 3D models' predictions of fibre moment arms,

inclusion of the detailed sarcomere length distribution information could improve our confidence in the force predictions from the finite element models and enable us to compare predictions of force between finite element and line-segment models.

To develop a model that was representative of normal, healthy shoulders, we collected imaging data from an average-sized, healthy young adult. Previous shoulder models have been derived from either the visible human project (Garner and Pandy 2001; Teran et al. 2005; Charlton and Johnson 2006; Blana et al. 2008, 2009; Yanagawa et al. 2008) or cadaveric data (van der Helm 1994; Holzbaur et al. 2005; Holzbaur et al. 2007). The visible human subject was large and highly muscular, whereas cadaveric specimens often suffer from atrophy. Therefore, one would expect that some of the differences between our results and other studies would be due to these different subject populations.

The 3D finite element models described here provide realistic representations of shoulder muscle lines of action and allowed examination of effects of contact, broad attachment and complex fibre arrangements on shoulder muscle actions. Although line-segment models represent muscle geometry well in some positions, they do not represent the variation in moment arms across fibres within a muscle, nor do they accurately reflect the effects of mechanical coupling between muscle compartments. This study demonstrates the potential for using 3D models to capture the complex 3D mechanical function of shoulder muscles.

Acknowledgements

We thank Garry Gold, M.D. for his assistance in gathering the MRI data and Jeff Weiss and Steve Maas for their assistance with the finite element modelling. This study was supported by a NSF Graduate Fellowship and NIH Grants R01EB006735, U54 GM072970 and R24 HD065690.

References

- An KN, Takahashi K, Harrigan TP, Chao EY. 1984. Determination of muscle orientations and moment arms. *J Biomech Eng.* 106(3):280–282.
- Blana D, Hincapie JG, Chadwick EK, Kirsch RF. 2008. A musculoskeletal model of the upper extremity for use in the development of neuroprosthetic systems. *J Biomech.* 41(8):1714–1721.
- Blana D, Kirsch RF, Chadwick EK. 2009. Combined feedforward and feedback control of a redundant, nonlinear, dynamic musculoskeletal system. *Med Biol Eng Comput.* 47(5):533–542.
- Blemker SS, Asakawa DS, Gold GE, Delp SL. 2007. Image-based musculoskeletal modeling: applications, advances, and future opportunities. *J Magn Reson Imaging.* 25(2):441–451.
- Blemker SS, Delp SL. 2005. Three-dimensional representation of complex muscle architectures and geometries. *Ann Biomed Eng.* 33(5):661–673.
- Blemker SS, Delp SL. 2006. Rectus femoris and vastus intermedius fiber excursions predicted by three-dimensional muscle models. *J Biomech.* 39(8):1383–1391.
- Blemker SS, Pinsky PM, Delp SL. 2005. A 3D model of muscle reveals the causes of nonuniform strains in the biceps brachii. *J Biomech.* 38(4):657–665.
- Charlton IW, Johnson GR. 2006. A model for the prediction of the forces at the glenohumeral joint. *Proc Inst Mech Eng H.* 220(8):801–812.
- Criscione JC, Douglas AS, Hunter WC. 2001. Physically based strain invariant set for materials exhibiting transversely isotropic behavior. *J Mech Phys Solids.* 49(4):871–897.
- de Groot JH, Brand R. 2001. A three-dimensional regression model of the shoulder rhythm. *Clin Biomech (Bristol, Avon).* 16(9):735–743.
- Epstein M, Wong M, Herzog W. 2006. Should tendon and aponeurosis be considered in series? *J Biomech.* 39(11):2020–2025.
- Fernandez JW, Mithraratne P, Thrupp SF, Tawhai MH, Hunter PJ. 2004. Anatomically based geometric modelling of the musculo-skeletal system and other organs. *Biomech Model Mechanobiol.* 2(3):139–155.
- Galban CJ, Maderwald S, Uffmann K, de Greiff A, Ladd ME. 2004. Diffusive sensitivity to muscle architecture: a magnetic resonance diffusion tensor imaging study of the human calf. *Eur J Appl Physiol.* 93(3):253–262.
- Garner BA, Pandy MG. 2001. Musculoskeletal model of the upper limb based on the visible human male dataset. *Comput Methods Biomech Biomed Eng.* 4(2):93–126.
- Gatti CJ, Dickerson CR, Chadwick EK, Mell AG, Hughes RE. 2007. Comparison of model-predicted and measured moment arms for the rotator cuff muscles. *Clin Biomech (Bristol, Avon).* 22(6):639–644.
- Halloran JP, Ackermann M, Erdemir A, van den Bogert AJ. 2010. Concurrent musculoskeletal dynamics and finite element analysis predicts altered gait patterns to reduce foot tissue loading. *J Biomech.* 43(14):2810–2815.
- Halloran JP, Erdemir A, van den Bogert AJ. 2009. Adaptive surrogate modeling for efficient coupling of musculoskeletal control and tissue deformation models. *J Biomech Eng.* 131(1):011014.
- Hallquist JO, Goudreau GL, Bension DJ. 1985. Sliding interfaces with contact-impact in large-scale lagrangian computations. *Int J Numer Methods Eng.* 51:107–137.
- Hincapie JG, Blana D, Chadwick EK, Kirsch RF. 2008. Musculoskeletal model-guided, customizable selection of shoulder and elbow muscles for a C5 SCI neuroprosthesis. *IEEE Trans Neural Syst Rehabil Eng.* 16(3):255–263.
- Holzbaur KR, Murray WM, Delp SL. 2005. A model of the upper extremity for simulating musculoskeletal surgery and analyzing neuromuscular control. *Ann Biomed Eng.* 33(6):829–840.
- Holzbaur KR, Murray WM, Gold GE, Delp SL. 2007. Upper limb muscle volumes in adult subjects. *J Biomech.* 40(4):742–749.
- Hughes RE, Niebur G, Liu J, An KN. 1998. Comparison of two methods for computing abduction moment arms of the rotator cuff. *J Biomech.* 31(2):157–160.
- Huijing PA. 1999. Muscle as a collagen fiber reinforced composite: a review of force transmission in muscle and whole limb. *J Biomech.* 32(4):329–345.
- Huijing PA, Baan GC. 2001. Extramuscular myofascial force transmission within the rat anterior tibial compartment: proximo-distal differences in muscle force. *Acta Physiol Scand.* 173(3):297–311.

- Inman VT, Saunders JBD, Abbott LC. 1944. Observations on the function of the shoulder joint. *J Bone Joint Surg.* 26:1–30.
- Kim SY, Boynton EL, Ravichandiran K, Fung LY, Bleakney R, Agur AM. 2007. Three-dimensional study of the musculo-tendinous architecture of supraspinatus and its functional correlations. *Clin Anat.* 20(6):648–655.
- Laursen TA, Maker BN. 1995. An augmented Lagrangian quasi-Newton solver for constrained nonlinear finite-element applications. *Int J Numer Methods Eng.* 38(21):3571–3590.
- Lemos RR, Epstein M, Herzog W. 2008. Modeling of skeletal muscle: the influence of tendon and aponeuroses compliance on the force-length relationship. *Med Biol Eng Comput.* 46(1):23–32.
- Liu J, Hughes RE, Smutz WP, Niebur G, Nan-An K. 1997. Roles of deltoid and rotator cuff muscles in shoulder elevation. *Clin Biomech (Bristol, Avon).* 12(1):32–38.
- Llewellyn ME, Barretto RPJ, Delp SL, Schnitzer MJ. 2008. Minimally invasive high-speed imaging of sarcomere contractile dynamics in mice and humans. *Nature.* 454(7205):784–788.
- Lu YT, Zhu HX, Richmond S, Middleton J. 2011. Modelling skeletal muscle fibre orientation arrangement. *Comput Methods Biomech Biomed Eng.* 14(12):1079–1088.
- Maas H, Baan GC, Huijing PA. 2001. Intermuscular interaction via myofascial force transmission: effects of tibialis anterior and extensor hallucis longus length on force transmission from rat extensor digitorum longus muscle. *J Biomech.* 34(7):927–940.
- Meskers CG, van der Helm FC, Rozendaal LA, Rozing PM. 1998. *In vivo* estimation of the glenohumeral joint rotation center from scapular bony landmarks by linear regression. *J Biomech.* 31(1):93–96.
- Napadow VJ, Chen Q, Mai V, So PT, Gilbert RJ. 2001. Quantitative analysis of three-dimensional-resolved fiber architecture in heterogeneous skeletal muscle tissue using nmr and optical imaging methods. *Biophys J.* 80(6):2968–2975.
- Oberhofer K, Mithraratne K, Stott NS, Anderson IA. 2009. Anatomically-based musculoskeletal modeling: prediction and validation of muscle deformation during walking. *Vis Comput.* 25(9):843–851.
- Otis JC, Jiang CC, Wickiewicz TL, Peterson MG, Warren RF, Santner TJ. 1994. Changes in the moment arms of the rotator cuff and deltoid muscles with abduction and rotation. *J Bone Joint Surg Am.* 76(5):667–676.
- Pappas GP, Asakawa DS, Delp SL, Zajac FE, Drace JE. 2002. Nonuniform shortening in the biceps brachii during elbow flexion. *J Appl Physiol.* 92(6):2381–2389.
- Prompers JJ, Jeneson JA, Drost MR, Oomens CC, Strijkers GJ, Nicolay K. 2006. Dynamic MRS and MRI of skeletal muscle function and biomechanics. *NMR Biomed.* 19(7):927–953.
- Puso MA, Maker BN, Ferencz RM, Hallquist JO. 2006. Nike3D: a non-linear, implicit, three-dimensional finite element code for solid and structural mechanics. Lawrence Livermore National Laboratory Technical Report. UCRL-MA-105268.
- Teran J, Sifakis E, Blemker SS, Ng-Thow-Hing V, Lau C, Fedkiw R. 2005. Creating and simulating skeletal muscle from the visible human data set. *IEEE Trans Vis Comput Graph.* 11(3):317–328.
- van der Helm FC. 1994. A finite element musculoskeletal model of the shoulder mechanism. *J Biomech.* 27(5):551–569.
- van der Helm FC, Veeger HE. 1996. Quasi-static analysis of muscle forces in the shoulder mechanism during wheelchair propulsion. *J Biomech.* 29(1):39–52.
- Van der Helm FC, Veeger HE, Pronk GM, Van der Woude LH, Rozendaal RH. 1992. Geometry parameters for musculoskeletal modelling of the shoulder system. *J Biomech.* 25(2):129–144.
- Van der Helm FC, Veenbaas R. 1991. Modelling the mechanical effect of muscles with large attachment sites: application to the shoulder mechanism. *J Biomech.* 24(12):1151–1163.
- van der Woude LH, Veeger HE, Dallmeijer AJ, Janssen TW, Rozendaal LA. 2001. Biomechanics and physiology in active manual wheelchair propulsion. *Med Eng Phys.* 23(10):713–733.
- Ward SR, Hentzen ER, Smallwood LH, Eastlack RK, Burns KA, Fithian DC, Friden J, Lieber RL. 2006. Rotator cuff muscle architecture: implications for glenohumeral stability. *Clin Orthop Relat Res.* 448:157–163.
- Weiss JA, Maker BN, Govindjee S. 1996. Finite element implementation of incompressible, transversely isotropic hyperelasticity. *Comput Methods Appl Mech Eng.* 135(1–2):107–128.
- Wu G, van der Helm FC, Veeger HE, Makhsous M, Van Roy P, Anglin C, Nagels J, Karduna AR, McQuade K, Wang X et al., 2005. ISB recommendation on definitions of joint coordinate systems of various joints for the reporting of human joint motion – Part II: shoulder, elbow, wrist and hand. *J Biomech.* 38(5):981–992.
- Yanagawa T, Goodwin CJ, Shelburne KB, Giphart JE, Torry MR, Pandy MG. 2008. Contributions of the individual muscles of the shoulder to glenohumeral joint stability during abduction. *J Biomech Eng.* 130(2):021024.
- Yucesoy CA, Koopman BH, Baan GC, Grootenboer HJ, Huijing PA. 2003. Effects of inter- and extramuscular myofascial force transmission on adjacent synergistic muscles: assessment by experiments and finite-element modeling. *J Biomech.* 36(12):1797–1811.
- Zajac FE. 1989. Muscle and tendon: properties, models, scaling, and application to biomechanics and motor control. *Crit Rev Biomed Eng.* 17(4):359–411.
- Zhou H, Novotny JE. 2007. Cine phase contrast MRI to measure continuum Lagrangian finite strain fields in contracting skeletal muscle. *J Magn Reson Imaging.* 25(1):175–184.